AGU PUBLICATIONS

Geophysical Research Letters

RESEARCH LETTER
10.1002/2017GL072570

Special Section:
First results from NASA's Magnetospheric Multiscale (MMS) Mission

Key Points:
- New algorithm enables determination of spacecraft trajectories through the magnetic reconnection diffusion region
- Crescent-shaped electron distributions occur at the location along the computed trajectory corresponding to the time MMS measured crescents

Supporting Information:
- Text S1
- Movie S1

Correspondence to:
J. R. Shuster,
jason.r.shuster@nasa.gov

Citation:
Shuster, J. R., et al. (2017), Hodographic approach for determining spacecraft trajectories through magnetic reconnection diffusion regions, *Geophys. Res. Lett.*, *44*, 1625–1633, doi:10.1002/2017GL072570.

Received 9 JAN 2017
Accepted 28 JAN 2017
Accepted article online 1 FEB 2017
Published online 16 FEB 2017

Hodographic approach for determining spacecraft trajectories through magnetic reconnection diffusion regions

J. R. Shuster[1,2,3], M. R. Argall[3], R. B. Torbert[3], L.-J. Chen[1], C. J. Farrugia[3], L. Alm[3], S. Wang[1,2], W. Daughton[4], D. J. Gershman[1,2], B. L. Giles[1], C. T. Russell[5], J. L. Burch[6], and C. J. Pollock[1]

[1]NASA Goddard Space Flight Center, Greenbelt, Maryland, USA, [2]Department of Astronomy, University of Maryland, College Park, Maryland, USA, [3]Space Science Center, University of New Hampshire, Durham, New Hampshire, USA, [4]Los Alamos National Laboratory, Los Alamos, New Mexico, USA, [5]Department of Earth, Planetary, and Space Sciences, University of California, Los Angeles, California, USA, [6]Southwest Research Institute, San Antonio, Texas, USA

Abstract We develop an algorithm that finds a trajectory through simulations of magnetic reconnection along which input Magnetospheric Multiscale (MMS) spacecraft observations are matched. Using two-dimensional particle-in-cell simulations of asymmetric reconnection, the method is applied to a magnetopause electron diffusion region (EDR) encountered by the MMS spacecraft to facilitate interpretation of the event based on fully kinetic models. The recently discovered crescent-shaped electron velocity distributions measured by MMS in the EDR are consistent with simulation distributions at the corresponding time along the computed trajectory.

1. Introduction

How can we infer a spacecraft's trajectory through the geometry of magnetic reconnection? Answering this question is crucial for interpreting satellite observations of reconnection in Earth's magnetosphere. Viewed from the frame of a reconnection *X* line at the magnetopause, the spacecraft's motion is often some complex, nonlinear path through the various reconnection regions.

The simplest attempt to orient spacecraft with respect to a theoretical model is to compare the spacecraft's measurements to a one-dimensional (1-D), linear slice through a simulation. This approach is reasonable provided the magnetopause can be modeled as a 1-D boundary whose velocity is large relative to the spacecraft, so that the satellite's path through the boundary is approximately straight. Many enlightening studies have employed this technique to interpret reconnection events using two-dimensional (2-D) particle-in-cell (PIC) simulations of reconnection [e.g., *Mozer et al.*, 2008; *Eastwood et al.*, 2010] and recently three-dimensional (3-D) simulations [e.g., *Chen et al.*, 2012; *Liu et al.*, 2013], where considering the spatial variation of quantities along a 1-D cut offers insight into the reconnection structure. A more realistic 1-D trajectory can be constructed using a nonlinear axis scaled by a local plasma parameter, as in *Mozer and Pritchett* [2009]. *Cattell et al.* [2005] studied the electron density cavities and bipolar parallel electric field structures along a path which followed a magnetic field line in a 2-D PIC simulation as a framework for examining Cluster observations of electron holes during magnetotail reconnection with a guide field. Considering the plasma density, magnetic field direction, and ion bulk velocity, *Muzamil et al.* [2014] inferred the Polar spacecraft's traversal of guide field reconnection structures in a new regime of extreme density asymmetry poleward of the cusp. Motivated by the structure of electron temperature anisotropy found in profiles through a PIC simulation of asymmetric reconnection, *Scudder et al.* [2012] reordered temporal measurements into a nonuniform spatial coordinate to interpret Polar's magnetopause electron diffusion region (EDR) crossing. Comparing maps of electron distribution functions measured by the four Cluster spacecraft to arrays of PIC distributions is another established technique for elucidating reconnection structures and processes, including magnetic islands and spatially extended electron current layers [*Chen et al.*, 2008], the temporal evolution stage of reconnection [*Shuster et al.*, 2014], and electron heating mechanisms in the reconnection exhaust [*Wang et al.*, 2016]. Most recently, *Burch et al.* [2016] and *Torbert et al.* [2016] reported an EDR encountered by the Magnetospheric Multiscale (MMS) spacecraft; using plasma and fields measurements, both studies included a sketch of the MMS tetrahedron's trajectory

through the EDR of a 2-D PIC domain, and *Torbert et al.* [2016] interpreted MMS signatures of energy dissipation using 1-D slices through the simulation of analogous quantities.

In each of these studies, spacecraft trajectories were inferred qualitatively by comparing bulk quantities and sometimes maps of electron distribution functions measured by the spacecraft to simulation predictions. In this paper, we approach the problem quantitatively by inputting spacecraft measurements to an algorithm which outputs a trajectory through the PIC simulation domain that matches the input data. We apply this method to acquire the MMS fleet's trajectory through the EDR encountered at the magnetopause on 16 October 2015 [*Burch et al.*, 2016; *Torbert et al.*, 2016]. We find crescent-shaped electron velocity distributions (studied in depth by *Chen et al.* [2016]) in the simulation at the location along the trajectory corresponding to the time at which MMS measured crescent structures.

2. Simulation Model

The particle-in-cell simulation we use models asymmetric magnetic reconnection with zero guide field in two spatial and three velocity dimensions. The boundary conditions are periodic in the outflow direction for fields and particles, while conducting for fields and reflecting for particles in the current sheet normal direction. Choosing the upstream magnetosphere (MSP) to magnetosheath (MSH) density ratio $n_{\mathrm{MSP}}/n_{\mathrm{MSH}} = 1/8$ and the initial MSH plasma beta $\beta_{\mathrm{MSH}} = 1$, the ratio of upstream magnetic field strengths is constrained to be $B_{\mathrm{MSP}}/B_{\mathrm{MSH}} \approx 1.37$. The domain is $L_x \times L_z = 75d_i \times 25d_i$ with 3072×2048 cells and an average of 3000 particles per cell, where d_i is the initial ion skin depth based on n_{MSH}. Additional parameters include the ion to electron mass ratio $m_i/m_e = 100$, temperature ratio $T_i/T_e = 2$, and initial MSH electron plasma to cyclotron frequency ratio $\omega_{pe}/\Omega_{ce} = c/v_{Ae,\mathrm{MSH}} = 2$ (where c is the speed of light and $v_{Ae,\mathrm{MSH}}$ is the initial MSH electron Alfvén speed). Reconnection is initiated by adding a perturbation to the magnetic field [*Daughton et al.*, 2014]. For more details regarding the simulation setup, please consult *Chen et al.* [2016] and references therein. The simulation data shown are from $t\Omega_{ci} = 68$ almost $10\Omega_{ci}^{-1}$ after the peak reconnection rate (where Ω_{ci} is the initial MSH ion cyclotron frequency). Unless noted, lengths are normalized to the initial MSH electron skin depth d_e, densities to n_{MSH}, and velocities to the speed of light c so that energies are in units of $m_e c^2$.

These initial conditions were chosen to approximately match the boundary conditions of the EDR event measured by MMS on 16 October 2015 around 13:00 UT. MMS observed the density ratio $n_{\mathrm{MSP}}/n_{\mathrm{MSH}} \approx 1\ \mathrm{cm}^{-3}/10\ \mathrm{cm}^{-3} = 1/10$, the upstream MSH plasma beta $\beta_{\mathrm{MSH}} = 2\mu_0 \cdot n_{\mathrm{MSH}} \cdot k(T_{i,\mathrm{MSH}} + T_{e,\mathrm{MSH}})/B_{\mathrm{MSH}}^2 \approx 1.2$ (using $T_{i,\mathrm{MSH}} = 250$ eV and $T_{e,\mathrm{MSH}} = 20$ eV), and the magnetic field ratio $B_{\mathrm{MSP}}/B_{\mathrm{MSH}} \approx 40$ nT/30 nT = 1.33. We note that there was likely a small guide field for this event ($B_g \approx 0.1B_{\mathrm{MSH}}$), though we do not expect this difference to adversely affect our results. We will discuss possible effects of the artificially small mass ratio and periodic outflow boundaries in section 5.

3. Trajectory-Finding Algorithm

In this section, we explain how the algorithm operates. First, the MMS data must be transformed to boundary-normal ("LMN") coordinates to compare with the simulation, where $+\hat{\mathbf{L}}$ is directed along the reconnection outflow, $+\hat{\mathbf{N}}$ points normal to the current sheet, and $+\hat{\mathbf{M}}$ completes a right-handed system. This transformation can be performed using several analysis methods, such as minimum variance of the magnetic field vector (MVAB) [*Sonnerup and Scheible*, 1998], minimum directional derivative analysis [*Shi et al.*, 2005], joint-variance analysis [*Mozer and Retinò*, 2007], or a combination of methods [*Denton et al.*, 2016].

Next, the algorithm takes as input a pair of normalized MMS quantities and returns a path through the simulation which matches the input data. Since two characteristic signatures of a diffusion region are the magnetic reversal in the reconnecting magnetic field component B_L and the ion flow reversal in U_{iL}, we chose these two quantities for the trajectory determination. Because of the symmetry of 2-D reconnection, the signs of B_L and U_{iL} roughly determine the quadrant of the L–N plane in which the trajectory location will reside.

Figure 1 shows a schematic illustrating the simple, iterative mechanism by which MMS measurements of B_L and U_{iL} are mapped into the PIC domain. The blue lines are contours of the PIC reconnecting component $B_L^{\mathrm{PIC}}(x, z, t_{\mathrm{PIC}})$, indicating all of the points in the domain at time t_{PIC} for which B_L^{PIC} is equal in magnitude to $\hat{B}_L^{\mathrm{MMS}}(t)$, the normalized reconnecting component observed by MMS at a particular time t. Likewise, the red lines are contours of the PIC ion outflow velocity $U_{iL}^{\mathrm{PIC}}(x, z, t_{\mathrm{PIC}})$ corresponding to $\hat{U}_{iL}^{\mathrm{MMS}}(t)$. As shown in the diagram, together these two contours can constrain the possible locations to a single point (green circle), namely,

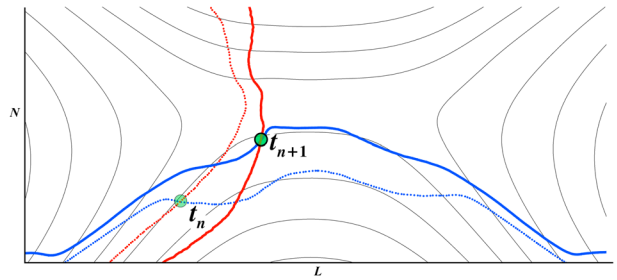

Figure 1. Schematic illustrating how the algorithm iteratively determines the spacecraft's location in the simulation domain. The dotted blue and red curves indicate contours of B_L^{PIC} and U_{iL}^{PIC}, respectively, corresponding to B_L^{MMS} and U_{iL}^{MMS} at time t_n, while the solid contours correspond to t_{n+1}. The intersection of these contours at time t_n, marked with green circles, gives the n*th* location (x_n, z_n) of the spacecraft's trajectory. The background black lines indicate contours of the magnetic flux function.

the intersection of the B_L^{PIC} (blue) and U_{iL}^{PIC} (red) contours. Choosing this location for the PIC spacecraft ensures that both B_L^{PIC} and U_{iL}^{PIC} will agree exactly with the observed B_L^{MMS} and U_{iL}^{MMS}. Figure 1 includes contours from two times, t_n (dotted) and t_{n+1} (solid), showing how data from consecutive times are used to trace a path through the simulation: spacecraft data at time t_n yield the intersection (x_n, z_n); repeating this procedure for t_{n+1}, t_{n+2}, etc., for each measurement during an entire time interval, the resulting trajectory will have the property that both $B_L^{\mathrm{PIC}}(x_n, z_n)$ and $U_{iL}^{\mathrm{PIC}}(x_n, z_n)$ match the observations at each t_n for $n = \{1, 2, \ldots\}$. This approach is equivalent to searching for the locations (x_n, z_n) in the simulation domain for each t_n which minimize the following residual expression:

$$\mathrm{error}(x, z, t) = \left|\hat{B}_L^{\mathrm{PIC}}(x, z) - \hat{B}_L^{\mathrm{MMS}}(t)\right| + \left|\hat{U}_{iL}^{\mathrm{PIC}}(x, z) - \hat{U}_{iL}^{\mathrm{MMS}}(t)\right| \tag{1}$$

For simplicity, we assume that the reconnection fields are steady by keeping the simulation time t_{PIC} fixed during the trajectory determination. We note that for complicated flow patterns (e.g., those that can form in association with large-scale magnetic islands), the above procedure can find more than one intersection between the B_L and U_{iL} contours. We avoid this situation by only considering simulation times at which one ion-scale *X* line has developed. Additional constraints of the algorithm can be used to choose between multiple intersections, such as minimizing the distance to the location determined from the previous time step, and minimizing the residuals of more than just B_L and U_{iL}.

4. Magnetopause Electron Diffusion Region Encounter

Here we apply the algorithm described above to gain insight into how the MMS tetrahedron may have traversed the EDR "caught" on 16 October 2015 around 13:07:02 UT [*Burch et al.*, 2016; *Denton et al.*, 2016; *Torbert et al.*, 2016]. MMS observed the reconnecting fields and particle distributions with unprecedented accuracy and time resolution: the FIELDS instrument suite measured a magnetic field vector 128 times per second [*Russell et al.*, 2014; *Torbert et al.*, 2014], and the Fast Plasma Investigation (FPI) measured a full plasma distribution function every 150 ms for ions and 30 ms for electrons [*Pollock et al.*, 2016].

4.1. Trajectory Determination

First, we rotate the MMS measurements to a boundary-normal coordinate system using the rotation matrix listed in Figure 1 of *Torbert et al.* [2016] determined via minimum variance analysis on the magnetic field (MVAB). In section 4.2, we also consider the LMN frame chosen by *Denton et al.* [2016] who used a combination of MVAB and minimum directional derivative analysis since the intermediate and minimum eigenvalues were not well separated for either method. For this event, we also added 100 km/s to the *L* velocity measurements $U_{iL,\mathrm{MMS}}$ and $U_{eL,\mathrm{MMS}}$ to account for the motion of the *X* line in the *L* direction as noted by *Denton et al.* [2016].

Figure 2 exhibits MMS 2 measurements and simulation quantities along the computed trajectory. Figure 2a shows MMS measurements (white points) of B_L plotted against U_{iL} during the 23 s interval from 13:06:47 UT to 13:07:10 UT and the matched simulation data (colored points, mostly covering the MMS points) corresponding to the trajectory in Figure 2b. The representation in Figure 2a is similar to the "hodograms" discussed by *Sonnerup and Scheible* [1998] and employed by *Hietala et al.* [2015]. The points in Figures 2a and 2b (small circles) are colored according to the color bar at the top of Figure 2c to indicate the passage of time. The virtual spacecraft starts in the MSH on the $-L$ side of the *X* line near $(L, N) \approx (340, 8)d_e$ (large green circle), samples the EDR on the MSP edge of the layer, and eventually leaves the EDR as $|B_L|$ increases near $(L, N) \approx (370, 12)d_e$ (large red circle). The gold stars indicate the time at which MMS 2, 3, and 4 observed crescent-shaped electron velocity distributions [*Burch et al.*, 2016] and will be addressed in the discussion for Figure 4. The remaining

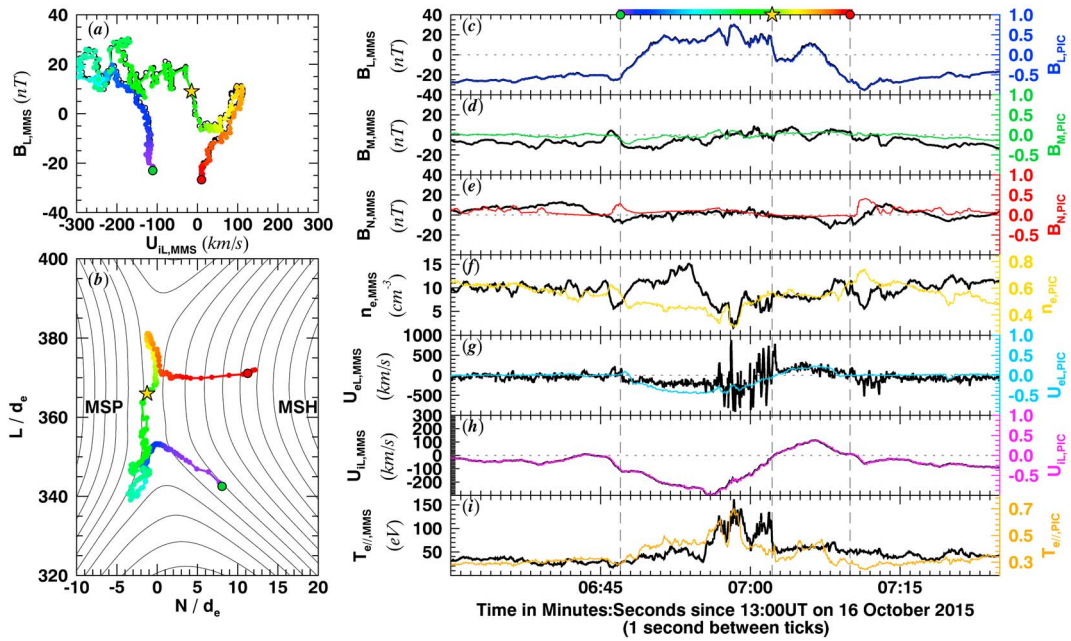

Figure 2. MMS 2 measurements and simulation quantities along the computed trajectory through the EDR. (a) MMS data in the B_L-U_{iL} plane with matched simulation quantities (colored by time) over plotted. (b) Computed trajectory of MMS 2 in the simulation *L*-*N* plane (colored by time). Seven quantities measured by MMS 2 (black) compared to simulation quantities (color) along the trajectory shown in Figure 2b: (c) *L* component, (d) *M* component, and (e) *N* component of the magnetic field; (f) electron density; *L* component of the (g) electron and (h) ion velocity; and (i) electron temperature parallel to the magnetic field. The larger green and red circles and the gold star in Figures 2a and 2b correspond to the times shown at the top of Figure 2c, and the colored bar is shown to indicate time along the trajectory. The gold star indicates the time when MMS 2 observed crescent structures in electron velocity distributions.

panels (Figures 2c–2i) show seven MMS quantities (black, left axes) compared to corresponding simulation quantities (color, right axes) taken along the computed trajectory. To simplify the PIC simulation units, we report the magnetic field strengths normalized by $0.8B_{\mathrm{MSH}}$, the electron density normalized by the initial MSH density n_{MSH}, the ion velocity normalized by $0.03c = 0.6v_{Ai,\mathrm{MSH}}$ (roughly the peak ion outflow velocity at this time), the electron velocity normalized by $0.3c = 0.6v_{Ae,\mathrm{MSH}}$ ($\sqrt{m_i/m_e} = 10$ times the ion velocity normalization), and the electron temperature by $0.15\ m_e c^2 = 0.6\ m_e v_{Ae,\mathrm{MSH}}^2$ (roughly the peak $T_{e//}$ on the MSP side).

By construction, the algorithm finds the trajectory through the simulation which matches the B_L and U_{iL} profiles observed by MMS, which is why there is almost no difference between MMS and simulation quantities in Figures 2a, 2c, and 2h. Each of the other simulation quantities has some features which are consistent with the spacecraft data and some which are different. The *M* component of the magnetic field (Figure 2d, green trace) shows less variation and is smaller in magnitude than the MMS data, likely because the simulation had no initial guide field. The *N* component (Figure 2e, red trace) agrees with MMS data during 13:06:49 UT to 13:07:07 UT but deviates from MMS near 13:06:47 UT and 13:07:12 UT when the trajectory is far from the $N = 0$ plane. The electron density (gold trace in Figure 2f) agrees well with MMS during 13:06:55 UT to 13:07:08 UT even following the dip in density near 13:06:58 UT but does not follow MMS as closely elsewhere. The *L* component of the electron velocity (Figure 2g, light blue trace) mostly agrees with MMS except for the interval from 13:06:56 UT to 13:07:03 UT where $U_{eL,\mathrm{MMS}}$ exhibits rapid, large-amplitude variations and significantly deviates from the ion velocity $U_{iL,\mathrm{MMS}}$, indicative of substructures within the EDR not captured by the 2-D simulation at this time. Lastly, in Figure 2i the electron temperature parallel to the magnetic field $T_{e\|}$ (orange trace) is consistent with MMS especially at the two peaks a few seconds before 13:07:00 UT associated with the density dip, though the peaks seen by MMS just after this time were missed.

4.2. Accuracy and Robustness

As a measure of the trajectory's overall accuracy, we calculate normalized differences between each simulation quantity, Q_i^{PIC}, shown in Figures 2c–2i and the corresponding MMS data, Q_i^{MMS}, averaged over the time interval

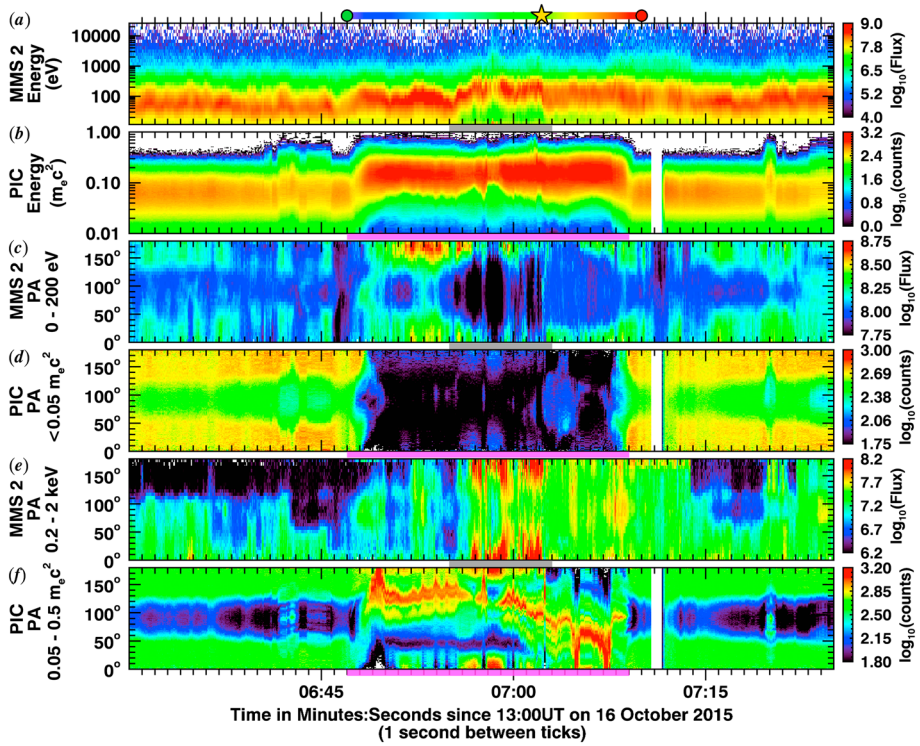

Figure 3. Electron spectrograms observed by MMS 2 with analogous PIC spectrograms calculated along the trajectory shown in Figure 2b: (a, b) omnidirectional energy spectrograms, (c, d) low-energy pitch angle spectrograms, and (e, f) mid-energy pitch angle spectrograms. The red and green circles, gold star, and colored time bar at the top of Figure 3a indicate the same times as in Figure 2. (Data were not available for the gap near 13:07:11 UT in Figures 3b, 3d, and 3f.)

shown: $\Delta Q_i = \left\langle \left| \hat{Q}_i^{\mathrm{PIC}} - \hat{Q}_i^{\mathrm{MMS}} \right| \right\rangle_t$. These residuals for each of the N quantities considered are then averaged together as a measure of the trajectory's total error: $\frac{1}{N}\sum_{i=1}^{N} \Delta Q_i$. For the seven quantities taken along the trajectory featured in Figure 2, this overall error is 8.9% (Figure S1 in the supporting information). During just the interval including the EDR from 13:06:53 UT to 13:07:05 UT the average error was about 9.1%, and at the time when MMS observed the crescent distributions (gold star) the error was 4.9%. As a basis for interpreting these numbers, the error of trajectories chosen by eye (without the algorithm) and interpolated to match the resolution of the MMS data ranged from 30% to 40%.

To further quantify the robustness of the algorithm, we explored how the output trajectory depends on the following: (1) simulation normalization B_0^{PIC} (from $0.7B_{\mathrm{MSH}}$ to $1.0B_{\mathrm{MSH}}$), (2) spacecraft data (MMS 2 versus MMS 3), (3) simulation time (after peak reconnection at $t\Omega_{ci} = 68$ to before at $t\Omega_{ci} = 56$), and (4) LMN frame (*Torbert et al.* [2016] compared to *Denton et al.* [2016]). For each test, the computed trajectories were similar to that shown in Figure 2. In (4), we used the LMN frame found by *Denton et al.* [2016] which differed from *Torbert et al.* [2016] by about 8.8° in L, 13.9° in M, and 10.7° in N (Figure S2).

4.3. Electron Spectrograms

After finding the trajectory, we are equipped to compare kinetic aspects of the MMS observations and simulations. In Figure 3, we compute simulation electron energy versus time and pitch angle versus time spectrograms to compare with FPI's dual electron spectrometers' (DES) data on MMS 2. To generate the PIC spectrograms, we select electrons from a bin of $1d_e \times 1d_e$ centered at each location along the trajectory. Figures 3a and 3b show the MMS and PIC omnidirectional energy-time spectrograms, respectively, while Figures 3c–3f show MMS and PIC pitch angle (PA) spectrograms: Figures 3c and 3d show low-energy electrons (0 to 200 eV for MMS and 0 to 0.05 $m_e c^2$ for PIC), while Figures 3e and 3f show a middle energy range (0.2 to 2 keV for MMS and 0.05 to 0.5 $m_e c^2$ for PIC). For reference, 1.0 $m_e c^2 = 4\, m_e v_{Ae,\mathrm{MSH}}^2$ for the simulation, while for the MMS observations 1 keV $\approx 2.24\, m_e v_{Ae,\mathrm{MSH}}^2$ (where $v_{Ae,\mathrm{MSH}} \approx 8{,}860$ km/s with $B_{\mathrm{MSH}} = 30$ nT and $n_{\mathrm{MSH}} = 10\ \mathrm{cm}^{-3}$).

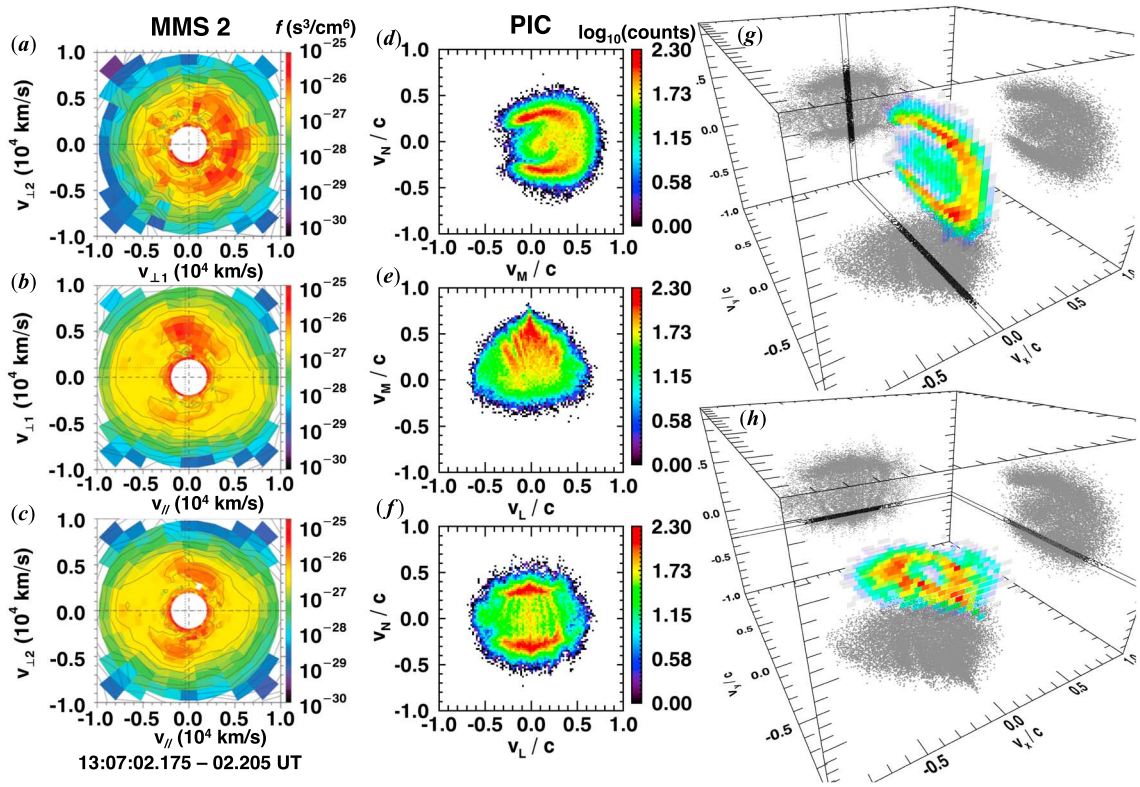

Figure 4. Crescent-shaped electron velocity distributions observed by MMS 2 and found in the simulation in the EDR at the time indicated by the gold star in Figures 2 and 3: MMS 2 distribution in the (a) $v_{\perp 1} - v_{\perp 2}$, (b) $v_{\parallel} - v_{\perp 1}$, and (c) $v_{\parallel} - v_{\perp 2}$ planes, where $v_{\perp 1}$ is the $\mathbf{E} \times \mathbf{B}$ direction (adapted from Figure 3 of *Burch et al.* [2016]); simulation distribution in the analogous (d) $v_M - v_N$, (e) $v_L - v_M$, and (f) $v_L - v_N$ planes; (g) $v_y - v_z$ and (h) $v_x - v_y$ slices of the distribution shown in Figures 4d–4f). (Movie S1 shows a more complete visualization of this 3-D velocity space structure.)

From 13:06:55 UT to 13:07:03 UT (marked by grey bars at the bottom of the MMS panels), the electron energy spectrogram measured by MMS (Figure 3a) shows significant electron energization up to a few keV (color in the MMS panels in Figures 3a, 3c, and 3e show energy flux in keV/[cm^2·s·str·keV]). This feature is seen as a drop in flux of low-energy electrons for all PAs except close to 0° and 180°. The energized electrons appear in the mid-energy PA spectrogram (Figure 3e) especially at 0° and 180°, which explains the $T_{e\parallel}$ peaks around this time (Figure 2i). Also of note are several discrete structures of increasing electron flux extending toward more perpendicular PAs. Comparing these observations with the PIC spectrograms, as with the bulk quantities along this trajectory, there are both similarities and differences. The PIC energy spectrogram (Figure 3b) shows significantly increased counts throughout energies ranging from about 0.05 to 0.5 $m_e c^2$, in qualitative agreement with MMS. However, the time interval of energization is longer, starting at near 13:06:47 UT and lasting until about 13:07:09 UT (marked by the magenta horizontal bars below the PIC panels). The decrease in electron counts for the PIC low-energy PA spectrogram (Figure 3d) appears as increased counts in the mid-energy PA spectrogram (Figure 3f) during this extended interval as was the case for MMS during the shorter interval. The distribution of PIC pitch angles, however, is more intricate than MMS observed: much of the PIC mid-energy electron PAs are predominantly centered in the range of 50° to 150° (e.g., from 13:06:51 UT to 13:07:03 UT), except a few times where parallel and antiparallel populations accompany the complicated perpendicular populations (e.g., from 13:06:56 UT to 13:06:59 UT).

4.4. Electron Velocity Distributions: Crescent Structures

The gold star was shown in Figures 2 and 3 because at this time MMS 2, 3, and 4 observed crescent-shaped electron velocity distributions, one of which from MMS 2 is displayed in Figures 4a–4c (reproduced in part from Figure 3 in *Burch et al.* [2016]) and compared to the PIC distribution in Figures 4d–4h taken at the corresponding location along the computed trajectory: $(x, z) = (365.96, 1.25)d_e$. The complicated, energized perpendicular electrons of the PIC mid-energy PA spectrogram (Figure 3f) correspond to these highly nongyrotropic crescent populations. At this time, the PIC magnetic field was mainly along $+\hat{\mathbf{L}}$ (see Figures 2c–2e),

so $v_{\parallel}^{\mathrm{MMS}} \rightarrow v_L^{\mathrm{PIC}}$. Additionally, the electric field was mostly along $+\hat{\mathbf{N}}$ (data not shown), so $v_{\perp 1}^{\mathrm{MMS}} \rightarrow v_M^{\mathrm{PIC}}$ since $v_{\perp 1}$ was defined to point in the $\hat{\mathbf{E}} \times \hat{\mathbf{B}}$ direction. Thus, $v_{\perp 2}^{\mathrm{MMS}} \rightarrow v_N^{\mathrm{PIC}}$.

The MMS $v_{\perp 1} - v_{\perp 2}$ distribution in Figure 4a shows a distinct crescent structure characteristic of accelerated MSH electrons measured on the MSP side of the EDR [*Hesse et al.*, 2014; *Chen et al.*, 2016]. The corresponding PIC distribution in $v_M - v_N$ (Figure 4d) has higher counts at the ends of its crescent around $\pm v_N \approx 0.3c = 0.60 v_{Ae,\mathrm{MSH}}$ and $v_M \approx 0$, whereas MMS measured the highest PSD values near $v_{\perp 2} \approx 0$ and $v_{\perp 1} \approx 0.5 \times 10^4$ km/s $= 0.56 v_{Ae,\mathrm{MSH}}$. Taking a slice of the PIC distribution in 3-D velocity space (Figure 4g), the crescent is more readily apparent. In the $v_L - v_M$ projection (Figure 4e) the PIC crescent appears as a population centered around $v_L \approx -0.05c = -0.10 v_{Ae,\mathrm{MSH}}$ and $v_M \approx 0.5c = 1.0 v_{Ae,\mathrm{MSH}}$, qualitatively consistent with the MMS distribution (Figure 4b) whose main population is centered at $v_{\parallel} \approx -0.1 \times 10^4$ km/s $= -0.11 v_{Ae,\mathrm{MSH}}$ and $v_{\perp 1} \approx 0.5 \times 10^4$ km/s $= 0.56\, v_{Ae,\mathrm{MSH}}$. The PIC distribution resolves numerous discrete structures resembling a "leaf" shape as described by *Chen et al.* [2016], while the MMS distribution has a weaker, counterstreaming component near $v_{\perp 1} \approx -0.4 \times 10^4$ km/s $= -0.45 v_{Ae,\mathrm{MSH}}$ absent from the PIC distribution. Fewer discrete structures are contained in a slice through one of the v_N lobes (Figure 4h). Both the MMS $v_{\parallel} - v_{\perp 2}$ distribution (Figure 4c) and the corresponding PIC $v_L - v_N$ distribution (Figure 4f) exhibit counterstreaming electrons in $\pm v_N$ ($\pm v_{\perp 2}$) and a faint background population heated in v_L ($v_{\parallel}$). Movie S1, from which Figures 4g and 4h were derived, thoroughly "dissects" the distribution offering an illuminating visualization of the multiple, embedded structures. These discrete populations are reminiscent of the swirling striations in the triangular EDR distributions studied by *Bessho et al.* [2014] and *Shuster et al.* [2015] for symmetric reconnection. Here in the asymmetric case, the bifurcated structure in v_N ($v_{\perp 2}$) is connected via the crescents, which results in a "filled-in" $N - v_N$ phase-space (Figure S3) rather than the phase-space-hole structure that can form in the symmetric configuration [*Chen et al.*, 2011].

5. Discussion and Conclusions

We develop an algorithm to find "best fit" trajectories through simulation domains that minimize the residual between spacecraft measurements and simulation data. Inputting the L component of the magnetic field (B_L) and ion bulk velocity (U_{iL}) observed by MMS during a magnetopause EDR crossing, and using 2-D PIC simulations of asymmetric reconnection, we compute trajectories that match the input MMS data. We tested the algorithm's sensitivity to the simulation normalization, time, spacecraft number, and rotation of the MMS boundary-normal (LMN) frame.

Applying the algorithm to MMS data during the time interval closest to the EDR crossing, the virtual spacecraft made the following observations consistent with MMS measurements: (1) crescent-shaped electron distributions with qualitatively similar features in three projections of the $v_{\parallel} - v_{\perp 1} - v_{\perp 2}$ velocity space, (2) omnidirectional energy spectrograms exhibiting electron energization throughout the EDR, (3) pitch angle spectrograms showing increased flux of energized, counterstreaming electrons at 0° and 180° with discrete populations appearing in the perpendicular directions, and (4) qualitative agreement in several other quantities, including a density dip near 13:06:58 UT correlated with peaks in $T_{e\parallel}$, and an electron flow reversal during 13:06:57 UT to 13:07:03 UT. While there are discrepancies along the trajectory, the overall error is about 9% and only 5% at the time when MMS observed the crescent distributions in the EDR.

Slices of the PIC distributions in 3-D velocity space are somewhat more consistent with MMS measurements, possibly because FPI also measures "slices" of the total plasma population. We speculate that the new "parallel crescents" reported in *Burch et al.* [2016] are related to the "swirling" spatial evolution of the distribution function downstream of the X line where the v_L electron jets enhance, a region which MMS could have sampled after passing by the magnetic null. This evolution is studied in detail by *Shuster et al.* [2015] for symmetric reconnection and recently by *Chen et al.* [2016] in the asymmetric case.

The extended temporal duration of the electron energization region encountered by the virtual spacecraft (Figure 4b) compared to that measured by MMS (Figure 4a) is likely due to the simulation's artificial mass ratio $m_i/m_e = 100$. The size of the simulation EDR (on the order of d_e) relative to the size of the ion diffusion region (on the order of d_i) is roughly four times larger than in reality, since $(d_e/d_i)_{\mathrm{PIC}} = \sqrt{m_e/m_i} = \sqrt{1/100} = 0.1$, while in reality $(d_e/d_i) = \sqrt{1/1836} = 0.023$. Additionally, the periodic outflow boundary conditions could explain the presence of counterstreaming electrons in the simulation pitch angle spectrograms (Figures 3d and 3f) which are not observed by MMS (Figure 3e) before 13:06:47 UT and after 13:07:09 UT.

There are several ways to improve the algorithm we developed. One is to extend the procedure to 3-D simulations, where "contours" would become surfaces and the computed trajectory would match three measured quantities (e.g., the full magnetic field vector B_L, B_M, and B_N). The 3-D version of this algorithm would in principle resemble the technique developed by *Komar et al.* [2013] for efficiently tracing separators in 3-D global MHD simulations; only rather than searching for nulls along a separator, the algorithm would search for regions of the magnetic topology which correspond to input spacecraft data. Another improvement would be to relax the assumption that the reconnection structure does not change in time, allowing the simulation to evolve in the course of the trajectory determination. If in this process we find a particular time evolution which reduces the total error considerably, we could use this information to infer the reconnection rate of the event observed by the spacecraft. Such improvements are underway in anticipation of continued MMS discoveries that will further strengthen our understanding of the electron-scale phenomena fueling magnetic reconnection.

Acknowledgments
This research was supported in part by NSF grants AGS-1543598, AGS-1202537, AGS-1552142; NASA Earth and Space Science Fellowship (NESSF); NASA grants to the Theory and Modeling Program, FIELDS team; and the Fast Plasma Investigation of the MMS mission. The simulation data are available upon request from the authors. We especially thank the MMS instrument teams for their outstanding engineering and determination, which has culminated in the delivery of such exceptional data, available to the public via https://lasp.colorado.edu/mms/sdc/public/.

References

Bessho, N., L.-J. Chen, J. R. Shuster, and S. Wang (2014), Electron distribution functions in the electron diffusion region of magnetic reconnection: Physics behind the fine structures, *Geophys. Res. Lett.*, *41*, 8688–8695, doi:10.1002/2014GL062034.

Burch, J. L., et al. (2016), First electron-scale measurements of magnetic reconnection in space, *Science*, *352*, aaf2939, doi:10.1126/science.aaf2939.

Cattell, C., et al. (2005), Cluster observations of electron holes in association with magnetotail reconnection and comparison to simulations, *J. Geophys. Res.*, *110*, A01211, doi:10.1029/2004JA010519.

Chen, L.-J., et al. (2008), Evidence of an extended electron current sheet and its neighboring magnetic island during magnetotail reconnection, *J. Geophys. Res.*, *113*, A12213, doi:10.1029/2008JA013385.

Chen, L.-J., W. S. Daughton, B. Lefebvre, and R. B. Torbert (2011), The inversion layer of electric fields and electron phase-space-hole structure during two-dimensional collisionless magnetic reconnection, *Phys. Plasmas*, *18*, 012904, doi:10.1063/1.3529365.

Chen, L.-J., W. Daughton, A. Bhattacharjee, R. B. Torbert, V. Roytershteyn, and N. Bessho (2012), In-plane electric fields in magnetic islands during collisionless magnetic reconnection, *Phys. Plasmas*, *19*, 112902, doi:10.1063/1.4767645.

Chen, L.-J., M. Hesse, S. Wang, N. Bessho, and W. Daughton (2016), Electron energization and structure of the diffusion region during asymmetric reconnection, *Geophys. Res. Lett.*, *43*, 2405–2412, doi:10.1002/2016GL068243.

Daughton, W., T. K. M. Nakamura, H. Karimabadi, V. Roytershteyn, and B. Loring (2014), Computing the reconnection rate in turbulent kinetic layers by using electron mixing to identify topology, *Phys. Plasmas*, *21*, 052307, doi:10.1063/1.4875730.

Denton, R. E., B. U. Ö. Sonnerup, H. Hasegawa, T. D. Phan, C. T. Russell, R. J. Strangeway, B. L. Giles, D. Gershman, and R. B. Torbert (2016), Motion of the MMS spacecraft relative to the magnetic reconnection structure observed on 16 October 2015 at 1307 UT, *Geophys. Res. Lett.*, *43*, 5589–5596, doi:10.1002/2016GL069214.

Eastwood, J. P., T. D. Phan, M. Øieroset, and M. A. Shay (2010), Average properties of the magnetic reconnection ion diffusion region in the Earth's magnetotail: The 2001–2005 Cluster observations and comparison with simulations, *J. Geophys. Res.*, *115*, A08215, doi:10.1029/2009JA014962.

Hietala, H., J. F. Drake, T. D. Phan, J. P. Eastwood, and J. P. McFadden (2015), Ion temperature anisotropy across a magnetotail reconnection jet, *Geophys. Res. Lett.*, *42*, 7239–7247, doi:10.1002/2015GL065168.

Hesse, M., N. Aunai, D. Sibeck, and J. Birn (2014), On the electron diffusion region in planar, asymmetric, systems, *Geophys. Res. Lett.*, *41*, 8673–8680, doi:10.1002/2014GL061586.

Komar, C. M., P. A. Cassak, J. C. Dorelli, A. Glocer, and M. M. Kuznetsova (2013), Tracing magnetic separators and their dependence on IMF clock angle in global magnetospheric simulations, *J. Geophys. Res. Space Physics*, *118*, 4998–5007, doi:10.1002/jgra.50479.

Liu, Y.-H., W. Daughton, H. Karimabadi, H. Li, and V. Roytershteyn (2013), Bifurcated structure of the electron diffusion region in three-dimensional magnetic reconnection, *Phys. Rev. Lett.*, *110*, 265004, doi:10.1103/PhysRevLett.110.265004.

Mozer, F. S., and P. L. Pritchett (2009), Regions associated with electron physics in asymmetric magnetic field reconnection, *Geophys. Res. Lett.*, *36*, L07102, doi:10.1029/2009GL037463.

Mozer, F. S., and A. Retinò (2007), Quantitative estimates of magnetic field reconnection properties from electric and magnetic field measurements, *J. Geophys. Res.*, *112*, A10206, doi:10.1029/2007JA012406.

Mozer, F. S., P. L. Pritchett, J. Bonnell, D. Sundkvist, and M. T. Chang (2008), Observations and simulations of asymmetric magnetic field reconnection, *J. Geophys. Res.*, *113*, A00C03, doi:10.1029/2008JA013535.

Muzamil, F. M., C. J. Farrugia, R. B. Torbert, P. R. Pritchett, F. S. Mozer, J. D. Scudder, C. T. Russell, P. E. Sandholt, and L. B. Wilson III (2014), Structure of a reconnection layer poleward of the cusp: Extreme density asymmetry and a guide field, *J. Geophys. Res. Space Physics*, *119*, 7343–7362, doi:10.1002/2014JA019879.

Pollock, C. J., et al. (2016), Fast plasma investigation for magnetospheric multiscale, *Space Sci. Rev.*, *199*, 331–405, doi:10.1007/s11214-016-0245-4.

Russell, C. T., et al. (2014), The magnetospheric multiscale magnetometers, *Space Sci. Rev.*, *199*, 189–256, doi:10.1007/s11214-014-0057-3.

Scudder, J. D., R. D. Holdaway, W. S. Daughton, H. Karimabadi, V. Roytershteyn, C. T. Russell, and J. Y. Lopez (2012), First resolved observations of the demagnetized electron-diffusion region of an astrophysical magnetic-reconnection site, *Phys. Rev. Lett.*, *108*, 225005, doi:10.1103/PhysRevLett.108.225005.

Shi, Q. Q., C. Shen, Z. Y. Pu, M. W. Dunlop, Q.-G. Zong, H. Zhang, C. J. Xiao, Z. X. Liu, and A. Balogh (2005), Dimensional analysis of observed structures using multipoint magnetic field measurements: Application to Cluster, *Geophys. Res. Lett.*, *32*, L12105, doi:10.1029/2005GL022454.

Shuster, J. R., L.-J. Chen, W. S. Daughton, L. C. Lee, K. H. Lee, N. Bessho, R. B. Torbert, G. Li, and M. R. Argall (2014), Highly structured electron anisotropy in collisionless reconnection exhausts, *Geophys. Res. Lett.*, *41*, 5389–5395, doi:10.1002/2014GL060608.

Shuster, J. R., L.-J. Chen, M. Hesse, M. R. Argall, W. Daughton, R. B. Torbert, and N. Bessho (2015), Spatiotemporal evolution of electron characteristics in the electron diffusion region of magnetic reconnection: Implications for acceleration and heating, *Geophys. Res. Lett.*, *42*, 2586–2593, doi:10.1002/2015GL063601.

Sonnerup, B. U. Ö., and M. Scheible (1998), Minimum and maximum variance analysis, in *Analysis Methods for Multi-Spacecraft Data, ISSI Sci. Rep. SR-001*, edited by G. Paschmann and P. W. Daly, pp. 185–220, ISSI/ESA, Noordwijk, Netherlands.

Torbert, R. B., et al. (2014), The FIELDS instrument suite on MMS: Scientific objectives, measurements, and data products, *Space Sci. Rev.*, *199*, 105–135, doi:10.1007/s11214-014-0109-8.

Torbert, R. B., et al. (2016), Estimates of the terms in Ohm's law during an encounter with an electron diffusion region, *Geophys. Res. Lett.*, *43*, 5918–5925, doi:10.1002/2016GL069553.

Wang, S., L.-J. Chen, N. Bessho, L. M. Kistler, J. R. Shuster, and R. Guo (2016), Electron heating in the exhaust of magnetic reconnection with negligible guide field, *J. Geophys. Res. Space Physics*, *121*, 2104–2130, doi:10.1002/2015JA021892.